Clim. Past Discuss., 9, 4771–4806, 2013
www.clim-past-discuss.net/9/4771/2013/
doi:10.5194/cpd-9-4771-2013

Climate of the Past
Discussions
Open Access

Hindcasting the continuum of Dansgaard–Oeschger variability: mechanisms, patterns and timing

L. Menviel[1,2], A. Timmermann[3], T. Friedrich[3], and M. H. England[1,2]

[1]Climate Change Research Centre, University of New South Wales, Sydney, Australia
[2]ARC Centre of Excellence in Climate System Science, Australia
[3]International Pacific Research Center, School of Ocean and Earth Sciences and Technology, University of Hawai'i at Mānoa, Honolulu, Hawaii, USA

Received: 26 July 2013 – Accepted: 7 August 2013 – Published: 16 August 2013

Correspondence to: L. Menviel (l.menviel@unsw.edu.au)

Published by Copernicus Publications on behalf of the European Geosciences Union.

Abstract

Millennial-scale variability associated with Dansgaard–Oeschger (DO) and Heinrich events (HE) is arguably one of the most puzzling climate phenomena ever discovered in paleoclimate archives. Here, we set out to elucidate the underlying dynamics by conducting a transient global hindcast simulation with a 3-dimensional intermediate complexity Earth system model covering the period 50 ka BP to 30 ka BP. The model is forced by time-varying external boundary conditions (greenhouse gases, orbital forcing, and ice sheet orography and albedo) and anomalous North Atlantic freshwater fluxes, which mimic the effects of changing Northern Hemisphere ice-volume on millennial timescales. Together these forcings generate a realistic global climate trajectory, as demonstrated by an extensive model/paleo data comparison. Our analysis is consistent with the idea that variations in ice sheet calving and related changes of the Atlantic Meridional Overturning Circulation were the main drivers for the continuum of DO and HE variability seen in paleorecords across the globe.

1 Introduction

The glacial climate system during Marine Isotope Stage 3 (MIS3, 60–24 ka BP) experienced massive variability on timescales of centuries and millennia. Characterized by rapid Northern Hemisphere transitions from cold (stadial) to warm (interstadial) conditions (Fig. 1, black line), a subsequent gradual cooling and sometimes final rapid transition to cold conditions (Dansgaard et al., 1993), this so-called Dansgaard–Oeschger (DO) variability is a prominent glacial climate feature that has not been fully explained yet. In spite of recent progress in reconstructing the global impacts of these events several key questions remain unanswered: (i) What processes determine the rapid transition from DO stadials to interstadials? (ii) What physical mechanisms govern the two-stage cooling? (iii) What sets the length of these events and their "periodicity"?

CPD
9, 4771–4806, 2013

To address these questions, we must first understand, which climate system components were actively involved in DO variability. A high-resolution ice-rafted debris (IRD) composite record from the Irminger and Iceland Sea cores SO82-5 (van Kreveld et al., 2000) and PS2644 (Voelker et al., 2000) (Fig. 1, upper panel, orange line) suggests that all DO stadials between 30–50 ka BP were accompanied by iceberg surges, which originated from the adjacent Northern Hemisphere ice sheets. Figure 1 shows that the IRD values (iceberg and freshwater fluxes) started to increase during interstadial periods and peaked at the end of the stadials, after which they decreased rapidly. During interstadial periods, iceberg calving increased, which led to changes in ocean circulation, sea-ice and a drop in surface temperatures over Greenland and elsewhere in the North Atlantic. This finding is consistent with the notion of a freshwater-driven throttling of oceanic convection (Sarnthein et al., 2001), meridional mass and heat transport and subsequent sea-ice expansion, which caused the gradual cooling during interstadials. Within the age uncertainties of northern North Atlantic IRD records relative to the Greenland temperature "template", Fig. 1 documents a tight relationship between DO variability and calving of icebergs, consistent with Bond and Lotti (1995) and Sarnthein et al. (2001).

In addition to DO-related IRD variability, there is widespread sedimentary evidence (Heinrich, 1988; Zahn et al., 1997; van Kreveld et al., 2000; Schönfeld et al., 2003b; Hemming, 2004; Hodell et al., 2010) for massive iceberg surges that originated mainly from the Laurentide ice sheet and extended far into the eastern North Atlantic (e.g. Grousset et al., 1993). These so-called Heinrich events released large amounts of freshwater into the North Atlantic, causing a weakening the Atlantic Meridional Overturning Circulation (AMOC), as suggested by paleoproxy data (Kissel et al., 2008; Sarnthein et al., 1995; Vidal et al., 1997; Zahn et al., 1997; Sarnthein et al., 2001) and numerous climate modeling experiments (Stouffer et al., 2007; Krebs and Timmermann, 2007a; Kageyama et al., 2013). Climate models further document that the corresponding changes in meridional oceanic heat transport, SST and atmospheric circulation are consistent with paleo data evidence of a interhemispheric temperature seesaw (Stenni et al., 2011), large-scale drying of the northern tropics (Wang et al., 2001; Deplazes et al., 2013) and increased precipitation in the Southern Hemisphere tropics (Garcin et al., 2006; Wang et al., 2007; Kanner et al., 2013).

What this simplified view of Heinrich events and the corresponding global teleconnections does not provide is an explanation for the abrupt transition from Heinrich stadials to interstadial conditions and for the fact that for some Heinrich events, the stadial cooling occurred prior to the peak IRD release (van Kreveld et al., 2000). This could suggest that freshwater discharges are not only driving AMOC variability, but that the state of the AMOC may also feed back to the various ice sheets, with effects on subsequent iceberg and freshwater release (Schulz et al., 1999; Timmermann et al., 2003; Shaffer et al., 2004; Alvarez-Solas et al., 2010; Marcott et al., 2011).

Based on their very distinctive sedimentological characteristics, Heinrich events have often been regarded as dynamically different from other DO interstadial/stadial transitions. However, given the fact that both were accompanied by (i) large-scale oceanic changes (Fig. 2), (ii) IRD layers (Fig. 1) and (iii) similar global teleconnections, *we hypothesize that Heinrich events and DO events are part of a continuum of variability that is generated through ice sheet/AMOC interactions.*

At this stage this is a rather general concept, that does not yet specify the nature of the internal and regional feedbacks, involving for instance sea-ice (Li et al., 2005, 2010; Petersen et al., 2013), changes of the atmospheric circulation (Wunsch, 2006; Eisenman et al., 2009), subsurface ocean warming (Shaffer et al., 2004; Krebs and Timmermann, 2007b; Alvarez-Solas et al., 2010) and corresponding ice sheet instabilities (Schoof, 2007; Menviel et al., 2010).

In this paper we set out to simulate the time-evolution of DO and Heinrich events for the period 50–30 ka BP using an intermediate complexity global climate model. We will compare the simulated variability with high-resolution paleoclimate reconstructions. The model simulation is based on the underlying assumption that the continuum of MIS3 climate variability on centennial to millennial timescales can be generated by a suitable North Atlantic freshwater forcing and the associated AMOC response.

The paper is organized as follows: in Sect. 2 the model and experimental setup are described. In Sect. 3 we discuss the patterns of variability as well as the abruptness and timing of DO events. We also derive a common age scale, that allows for a better comparison between paleoproxy records and model simulations. The paper concludes with a synthesis and discussion of the main results.

2 Model and experimental setup

One of the key goals of our study is to simulate the sequence of millennial-scale events during the period 50–30 ka BP and to determine the corresponding global teleconnections. For this task we have chosen the intermediate complexity Earth system model LOVECLIM (Timm and Timmermann, 2007; Menviel et al., 2008; Timmermann et al., 2009b; Goosse et al., 2010). The ocean component of LOVECLIM (CLIO) consists of a free-surface primitive equation model with a horizontal resolution of 3° longitude, 3° latitude, and 20 depth layers. The 3-dimensional atmospheric component (ECBilt) is a spectral T21, three-level model based on quasi-geostrophic equations of motion and ageostrophic corrections. LOVECLIM also includes a dynamic-thermodynamic sea-ice model, a land surface scheme, a dynamic global vegetation model (VECODE, Brovkin et al., 1997) and a marine carbon cycle model (LOCH, Menviel et al., 2008; Mouchet, 2011).

Initial conditions for the transient run were obtained by conducting an equilibrium spin-up simulation using an atmospheric CO_2 content of 207.5 ppmv, orbital forcing for the time 50 ka BP and an estimate of the 50 ka BP ice sheet orography and albedo which were obtained from a 130 ka off-line ice sheet model simulation (Abe-Ouchi et al., 2007). In the subsequent transient run greenhouse gases, orbital and ice sheet forcing were updated continuously following the methodology of Timm et al. (2008). Note that our coupled model does not include an interactive ice sheet. Therefore, freshwater withholding from the ocean during phases of ice sheet growth and freshwater release into the ocean as a result of ice sheet calving and ablation are not properly captured.

CPD
9, 4771–4806, 2013

To mimic the time-evolution of these terms and their effect on the ocean circulation, we apply an anomalous North Atlantic freshwater forcing $F(t)$ to the North Atlantic region 55° W–10° W, 50° N–65° N. Negative forcing anomalies can be interpreted as periods of ice sheet growth and excess evaporation over precipitation, whereas positive freshwater anomalies represent times of negative net mass balance of the Northern Hemisphere ice sheet, associated for instance with massive iceberg calving events or surface ablation.

The freshwater forcing time series $F(t)$ is obtained through an iterative procedure, that tries to optimize the anomalous freshwater flux such that the simulated temperature anomalies $T_s(t)$ in the eastern subtropical North Atlantic best match the target alkenone-based SST anomalies $T_r(t)$ reconstructed from the Iberian margin core MD01-2443 (Martrat et al., 2007) (Fig. 2, lower panel, orange line). Starting from an initial guess of the freshwater forcing $F_i(t) = -\alpha T_r(t)$, a series of about $j < 5$ experiments was conducted every 1000 yr using additional freshwater flux perturbations $\delta F^{(j)}(t)$. In each of these 1000 yr long chunks, the freshwater forcing scenario (j) was selected with $F^{(j)}(t) = F_i(t) + \delta F^{(j)}(t)$ that minimized the cost function

$$J^{(j)}(t) = \int_{t}^{t+\tau} \beta(T_s(t') - T_r(t'))^2 + \gamma(\dot{T}_s(t') - \dot{T}_r(t'))^2 \mathrm{d}t', \tag{1}$$

within this window $[t, t+\tau]$ with $\tau = 1000$ yr. The simulated temperature evolution for $T_s(t')$ in the integral is a function of the applied freshwater forcing $F^{(j)}(t')$. The resulting concatenated freshwater forcing timeseries $F(t)$ is shown in Fig. 2, upper panel. Similar to data-assimilation methods that adjust parameters and/or dynamical variables to reduce the mismatch between observations and models, $F(t)$ has the sole purpose to force LOVECLIM into a realistic trajectory with respect to millennial-scale subtropical North Atlantic SST anomalies during MIS3. We did not choose the Greenland temperature reconstruction as an optimization target, because it shows only very weak differences between DO and Heinrich stadials, in contrast to the North Atlantic SST reconstructions.

3 Results

3.1 Freshwater forcing

The applied North Atlantic freshwater forcing $F(t)$ captures the dominant meltwater pulses associated with the Heinrich events (HE5, HE4) (Fig. 2). It compares well with a recent freshwater forcing estimate (Jackson et al., 2010) obtained with a North Atlantic box model through Bayesian inversion methods[1]. In both cases stadial/interstadial transitions are triggered by negative forcing anomalies, which increase North Atlantic surface densities and subsequently strengthen the AMOC (Fig. 2, middle panel). Negative freshwater forcing can be interpreted to represent a positive ice sheet mass balance, which in our modeling framework mimics a reduction of the continental runoff as well as excess evaporation over precipitation over the North Atlantic region. As an independent validation of our freshwater forcing we compare the time-integral of $F(t)$, which represents the corresponding global sea level changes, with the composite IRD records from the Nordic Sea cores PS2644 and SO82-5 (Fig. 1) on the GICC05 timescale (see Sect. 3.6 for more details on the synchronization of the cores and the model results). The rationale of this comparison is that high values of IRD correspond to additional freshwater discharge and sea-level rise. Furthermore, rising sea level can amplify iceberg calving through ice-shelf instabilities. Except for the simulated sea-level rise associated with Heinrich event 5, which is not captured in these eastern North Atlantic paleorecords, we find a relatively good match between model simulation and

[1]Some discrepancies between $F(t)$ and the freshwater estimate of Jackson et al. (2010) arise from the different AMOC sensitivities to freshwater perturbations and the different choice of the optimization target (GISP2 for the box model (Jackson et al., 2010) and Iberian margin SST for LOVECLIM).

reconstruction, thus supporting the realism of the applied freshwater forcing. It should be noted here that the simulated DO-related sea level changes are a factor 2–3 smaller than those reconstructed from the Red Sea (Siddall et al., 2003).

3.2 AMOC response

As a result of the applied anomalous North Atlantic freshwater fluxes, the AMOC weakens and strengthens on millennial timescales. Heinrich stadials correspond to a complete shutdown of the AMOC transport, whereas DO stadials are associated with a 50 % weakening of the AMOC, relative to the interstadial periods (Fig. 2). The resulting AMOC timeseries compares reasonably well with a reconstruction of Atlantic bottom currents obtained from mass-normalized anhysteretic remanent magnetization (ARM) data (Kissel et al., 2008) (Fig. 2, middle panel), even though the model and paleoceanography timeseries are based on different underlying age models (a more detailed discussion of age-scale uncertainties is provided is Sect. 3.6).

3.3 Temperature response

The excellent agreement between simulated and reconstructed SST anomalies in the Iberian margin area (Fig. 2, lower panel) is to be expected, because the latter has been used as the target for the optimization of the freshwater fluxes. One important finding is that the temperature drop in the Northeast Atlantic around 36 ka BP (referred to as C7, adopting the Chapman and Shackleton (1999) terminology) can be obtained only by a complete shutdown of the AMOC, which is induced by a prolonged freshwater flux of ~ 0.1 Sv. This is consistent with the presence of an IRD pulse in the Greenland and Irminger Sea (see Fig. 1), a drop in sea surface salinity in SO82-5 (van Kreveld et al., 2000) and changes in benthic δ^{18}O (Margari et al., 2010). Whereas the IRD pulse is well pronounced in the composite IRD record (Fig. 1) as well as in marine sediment cores from the Southern Gardar Drift (JPC-13) (Hodell et al., 2010) and from the Iberian margin (MD95-2040) (Schönfeld et al., 2003a), it appears to be absent in

CPD
9, 4771–4806, 2013

MIS3 Heinrich and D/O

L. Menviel et al.

other southwestern Atlantic IRD records (e.g. Grousset et al., 1993; Rashid et al., 2003; Nave et al., 2007).

We move on to a more detailed comparison with other temperature reconstructions from the North Atlantic and Mediterranean realm. Figure 3 shows the comparison between simulated surface temperatures in Greenland and NGRIP temperature reconstructions (Huber et al., 2006) on the SS09 timescale. In accordance with paleo data, the simulated Heinrich and DO stadials have the same temperature level. This behavior in Greenland is quite distinct from SST reconstructions (Fig. 2 lower panel and Fig. 3 middle panel), which exhibit a marked difference between Heinrich and non-Heinrich stadials. These results indicate the presence of a nonlinear sea-ice feedback (Li et al., 2005; Deplazes et al., 2013) which saturates when sea-ice reaches a certain extent, thus capping cooling over Greenland. Simulated stadial/interstadial transitions attain values of about 9 °C in Greenland, which is smaller than the reconstructed values of up to 16 °C (Capron et al., 2010). Moreover, the simulation does not capture the slow interstadial cooling seen in the reconstructions. Instead interstadial periods have relatively constant Greenland temperatures in the model, except for an initial overshoot. This dynamics clearly differs from the behavior of SSTs in the northeastern Atlantic/Mediterranean (Figs. 2 and 3), which tracks the underlying AMOC variability much more accurately. Moving further into the eastern Mediterranean, we find a reasonable match between the simulated temperature anomalies in Turkey and the δ^{18}O record from independently-dated speleothems from Sofular cave (Fleitmann et al., 2009), which capture a combined temperature/hydroclimate signal.

A more comprehensive spatial view of the simulated DO/Heinrich event dynamics is obtained from an EOF analysis of global surface air temperatures (Fig. 4a). The dominant EOF mode is characterized by a meridional temperature seesaw in accordance with numerous other modeling studies (Stouffer et al., 2006, 2007; Timmermann et al., 2009a; Kageyama et al., 2013) and paleoclimate datasets (Blunier et al., 1998; Barker et al., 2009; Stenni et al., 2011). Interstadial conditions are characterized by Northern Hemisphere warming with strongest amplitudes over the Greenland-Iceland-

CPD
9, 4771–4806, 2013

Norway Sea and the Arctic Ocean. The warming extends into North Africa, Asia and the western North Pacific. The corresponding timeseries (Fig. 4c) clearly features the enhanced cooling during massive Heinrich stadials (Heinrich event 5,4) and the C7 event, in contrast to the weaker cooling associated with DO stadials. Simulated Southern Hemisphere cooling during interstadials is consistent with the presence of a bipolar temperature seesaw (Stocker, 1998; Stocker and Johnsen, 2003).

3.4 Hydroclimate response

As a result of the very strong North Atlantic cooling during Heinrich events (H5, H4) and during the C7 event (Fig. 3), Northern Hemisphere trade winds intensify by up to 60 %, which leads to a southward shift of the Intertropical Convergence Zones, extending from South America, into the tropical Atlantic, equatorial Africa and the Indian Ocean. This is illustrated by the EOF analysis of simulated precipitation in Fig. 4b and d.

The lower amplitude cooling during DO stadials weakens the trade winds by only 30 %. The corresponding southward shift of the tropical rainbands is less pronounced than for Heinrich events as shown by the leading principal component of the rainfall EOF analysis (Fig. 4d). In spite of a high correlation (0.92) between the principal components of temperature and rainfall, there are some notable differences. The precipitation mode exhibits a more pronounced two-step structure for the interstadial DO12 (around 47–46 ka) and a stronger difference between Heinrich stadials and DO stadials (Fig. 4d) than the temperature EOF mode (Fig. 4c). Qualitatively the patterns of simulated temperature and rainfall changes agree with those obtained from Coupled General Circulation Models subjected to North Atlantic freshwater perturbations (Broccoli et al., 2006; Timmermann et al., 2007; Kageyama et al., 2013).

Comparing the simulated Northern Hemisphere rainfall changes on a regional scale with hydroclimate reconstructions for Cariaco Basin (Deplazes et al., 2013), the Arabian Sea (Deplazes et al., 2013), eastern China (Wang et al., 2001) (Fig. 5) and Central America (Hodell et al., 2008) (Fig. 6, upper panel) we find an excellent agreement between model and data with stadial (interstadial) conditions corresponding to increased aridity (pluvials). The reverse pattern can be found for Southern Hemisphere hydroclimate proxies in Brazil (Wang et al., 2007), Peru (Kanner et al., 2013) and Ecuador (Mosblech et al., 2012) as well as for simulated rainfall changes (Fig. 6, lower three panels). In Sect. 3.6 we will try to reconcile some age-model discrepancies by projecting model and proxy data onto the common NGRIP GICC05 timescales (Andersen et al., 2006; Svensson et al., 2006).

3.5 Abruptness of events

To determine the response time of various climate variables and ocean transport indicators to freshwater changes, we calculate a composite (Fig. 7, black line) based on several stadial/interstadial DO transitions by aligning the model data relative to the maximum temperature derivative of the simulated Greenland temperature (47.25, 43.9, 41.8, 38.3, 35.3, 33.6, 32.34 ka BP). According to this analysis we find that the averaged DO transition takes place within 150 to 200 yr for all the climate variables in Fig. 7. However, for Greenland temperatures (Fig. 7a) and Northern Hemisphere sea-ice area (Fig. 7e), we see a considerable acceleration and an associated increase of abruptness 100 yr into the transition. This is in agreement with previous estimates of the abruptness of DO stadial/interstadial transitions in Greenland ice cores (~ 125 yr) (Capron et al., 2010), although much higher rates were reported in atmospheric circulation proxies (Steffensen et al., 2008).

As already demonstrated in Figs. 3 and 5 rainfall changes in the Cariaco basin area and the Arabian Sea clearly track millennial-scale SST variations in the North Atlantic region. This is further supported by the composite analysis which reveals a very similar time-evolution of these variables for the averaged DO stadial/interstadial transition. Rainfall changes in eastern China are less well pronounced owing to a much larger level of simulated rainfall variability that is unrelated to DO events.

According to Fig. 7h changes in the barotropic transport across the Indonesian archipelago occur almost in unison with the AMOC. This surprisingly fast adjustment can be attained by two processes: (i) wind changes in the Pacific (Timmermann et al.,

CPD
9, 4771–4806, 2013

2005b), (ii) fast oceanic adjustment processes involving wave propagation from the Atlantic into the Indian and Pacific Ocean, as discussed in Timmermann et al. (2005a). The former can modulate the Indonesian Throughflow via the Island Rule (Godfrey, 1989), whereas the latter would have to change the *Joint Effect of Baroclinicity and Relief* (JEBAR) term in the barotropic transport equation (Sarkisyan and Ivanov, 1971; Cane et al., 1998). Irrespective of the relative magnitudes of these terms, our analysis clearly documents that the DO variability has far-reaching fast oceanic impacts that extend also into the other ocean basins.

3.6 Common age scale

To better compare the paleorecords in Figs. 2, 3, 5 and the simulated climate variables, we make an attempt to bring them all onto the same age scale. We have chosen the Greenland Ice Core Chronology 2005 (GICC05) (Andersen et al., 2006; Svensson et al., 2006) as the common age model. To project the model simulation (30–50 ka BP) onto this age model, we compare the simulated Greenland temperature with the NGRIP $\delta^{18}O$ (Huber et al., 2006) and identify in a 1800 yr sliding window the lag at which the lag correlation attains its maximum value. Here we allow maximum lags of ±750 yr. To avoid large local discontinuities or reversals in the age model projection, we filtered the resulting timeseries of age-adjustments for the model simulation using a 500 yr running mean. The resulting Greenland temperature-based age-shift is then applied to all other model variables, thus keeping, at least to first order, the lead-lag structure within the model intact. We also project the sea surface salinity data from SO82-5 (van Kreveld et al., 2000), the ARM data and the Iberian Margin SST (Fig. 8) as well as the Cariaco and Arabian Sea color records (Fig. 9), onto the GICC05 timescale. Here we assume that at least in a 1800 yr sliding window, the proxy data varies in synchrony with the Greenland temperature record at zero lag. This assumption is well justified by the model results that show maximum correlation of 0.92 between the principal components of the leading EOFs of temperature (Fig. 4a and c) and precipitation (Fig. 4b and d) at zero lag. Furthermore, our model-based composite analysis of DO stadial/interstadial transitions supports the notion of near synchronicity (within ±100 yr) of the physical variables under consideration.

Having synchronized the model and paleoproxy data with the NGRIP $\delta^{18}O$ record on GICC05, we find a much better agreement between model and paleoproxy records, particularly for the period 50 to 40 ka BP. The ARM data now nicely features marked AMOC weakenings during H5, H4 and C7 as well as during most of the DO stadials (Fig. 8). In addition, the precipitation records from the Cariaco basin and the Arabian Sea are now in better agreement with the model, particularly for H5 (Fig. 9).

We conclude that if forced with a freshwater forcing that closely resembles (within the dating uncertainties) paleo salinity reconstructions from the Nordic Sea (Fig. 8) and a northern North Atlantic IRD composite (Fig. 1), the LOVECLIM model hindcast captures the dominant modes of Heinrich and DO variability found in paleo reconstructions. The model results further support that freshwater forcing triggered changes of the AMOC and North Atlantic SSTs, which subsequently caused the observed hydroclimate shifts across both hemispheres. This confirms our initial hypothesis that ice sheet instabilities played a crucial role in generating the continuum of millennial-scale DO/Heinrich variability in the North Atlantic during MIS3 (see also Sarnthein et al., 2001). Potential feedbacks of AMOC variability on the mass balance of the major ice sheets will be discussed in Sect. 4.

3.7 Timing and duration of events

Here we will take the opportunity to revisit the timing of some important climate events during MIS3. We will focus in particular on Heinrich stadials (H5, H4 and H3) and stadial event C7 (see Fig. 1) and use high resolution paleoclimate reconstructions with independent age control that capture Heinrich and DO variability. The event timing from NGRIP on GICC05 (Andersen et al., 2006), Sofular Cave, Turkey (Fleitmann et al., 2009), Pacupahuain Cave, Peru (Kanner et al., 2013), Santiago Cave, Ecuador (Mosblech et al., 2012) and Hulu Cave (Wang et al., 2001) is summarized in Table 1.

CPD
9, 4771–4806, 2013
MIS3 Heinrich and D/O
L. Menviel et al.

Consolidated estimates for the timing of H5, H4, C7 and H3 are 48.8–47.6 ka BP, 40.0–38.3 ka BP, 36.45–35.6 ka BP, and 31.3–28.8 ka BP, respectively. These ranges agree well with our model simulation (Figs. 2 and 3) but differ by up to 3 ka from recent sedimentological age estimates of Heinrich layers in marine sediment cores (Bond and Lotti, 1995; Vidal et al., 1999; Hemming, 2004).

The C7 stadial event was accompanied by a considerable IRD pulse in the northeastern North Atlantic, as seen for instance in the sediment cores PS2466, SO82-5, JPC-13 and MD95-2040. Furthermore, we find strongly reduced surface temperatures in the Atlantic and widespread Northern Hemisphere aridity (Figs. 2, 3 and 4). In our model simulation and in the paleoproxy data, the C7 stadial shares many common characteristics with the typical response for Heinrich events 3–5. In fact in the EOF analysis of the model simulation (Fig. 4) this period is basically indistinguishable from the other prominent Heinrich events, both in terms of temperature and rainfall. We therefore propose to introduce the term "Heinrich event 3.2" for this event, using the same nomenclature introduced for Heinrich event 5.2 (Sarnthein et al., 2001).

Paleorecords as well as the model results display little coherency regarding the amplitude and the timing of H3, which will be studied in details in a forthcoming study.

4 Conclusions

Here we presented a new transient model simulation that covers the period 30–50 ka BP. This climate model hindcast experiment was designed in such a way that freshwater forcing between 55° W–10° W, 50° N–65° N generated AMOC changes and subsequently northeastern Atlantic temperature anomalies that are agreement with alkenone-based temperature reconstructions from the Iberian margin area. With this weak constraint on model/data agreement, we were then able to independently evaluate the model performance with numerous other high-resolution climate proxies from both hemispheres. The resulting high level of agreement provides strong support for our initial hypothesis: Heinrich events and DO variability during MIS3 were caused by Northern Hemisphere ice sheet calving and freshwater discharges which subsequently influenced the strength of the AMOC, poleward heat transport and eventually global climate (Fig. 10). The qualitative agreement between the applied model freshwater perturbations, IRD records and salinity reconstructions from the Nordic Sea further highlights the realism of the LOVECLIM climate model hindcast and the applied forcing.

According to this ice sheet/AMOC scenario (Fig. 10), which follows some elements of Sarnthein et al. (2001), we suggest that ice sheet instabilities of low amplitude, originating mostly from the Eurasian, Iceland and Greenland ice sheets (Bond and Lotti, 1995), are the main driver of the fast DO variability. The corresponding low amplitude freshwater flux perturbations triggered a weakening of the AMOC, but not a complete collapse. We further acknowledge the possibility that DO climate variability may have caused ice sheet mass imbalances and calving from circum-Atlantic ice sheets (Bond and Lotti, 1995; Marshall and Koutnik, 2006), thus contributing to the DO-synchronized delivery of IRD into the North Atlantic. In contrast, instabilities from the Laurentide ice sheet occurred less frequently but were associated with much larger iceberg and freshwater discharges, leading to complete AMOC shutdown and larger SST and hydroclimate changes in the North Atlantic realm and beyond. Changes in sea-level during Heinrich events (Flückiger et al., 2006), and subsurface temperatures (Shaffer et al., 2004; Alvarez-Solas et al., 2010; Marcott et al., 2011) (Fig. 10) may have subsequently triggered marine-ice sheet instabilities, thus increasing the initial freshwater discharge. Such processes may have played a key role in synchronizing ice sheet dynamics in the Northern Hemisphere and in prolonging ice sheet instabilities during Heinrich events. Once the ice sheets reach a new mass-balance, the freshwater input into the North Atlantic ceases and the AMOC starts its recovery thus initiating a stadial/interstadial DO transition.

A more detailed view of the underlying mechanisms is provided in Fig. 11, which shows the time-evolution of the composite IRD record (Fig. 1) from cores SO82-5 and PS2644 (orange, upper curve), the salinity reconstruction (red) from Nordic Sea core SO82-5 (van Kreveld et al., 2000) and the GISP2 ice-core temperature reconstruction

CPD
9, 4771–4806, 2013

MIS3 Heinrich and D/O

L. Menviel et al.

(Alley, 2000). All data were interpolated onto the GICC05 timescales (see caption to Fig. 1 and Sect. 3.6 for more details). Here we begin with the high IRD values during H4, low salinities in the North Atlantic and a weak AMOC (40–39 ka BP). Around ~ 39 ka BP the strong freshwater forcing declines abruptly. Concomitantly, sea surface salinity increases thus initiating the AMOC recovery. The AMOC strengthening leads to Greenland and North Atlantic warming as well northern North Atlantic sea-ice retreat. Greenland Interstadial 8 (GIS8) is characterized by a very warm initial period which lasts for about 100–200 yr. IRD is at its minimum, North Atlantic surface salinity is high and so is the strength of the AMOC (Fig. 8). We consider this period of minimum ice sheet calving a period of positive Northern Hemisphere ice sheet mass balance, i.e growth. Around 37.5 ka BP calving resumes and increases until 37 ka BP. This evolution is briefly interrupted for about 100 yr between 36.9–36.8 ka BP, before a period of rapid iceberg surging and salinity decrease leads into the stadial cooling phase during H3.2. The stadial iceberg surging period lasts for 1 ka and comes to an end when the ice sheet calving has exhausted itself. This is the initiation of GIS7. The scenario outlined here for a set of paleoproxy datasets, is entirely consistent with the modeling-based evidence from Figs. 8 and 9.

Our paper further highlights the different response characteristics of various climate variables to AMOC changes (Fig. 7). The extraordinary abruptness of Greenland temperatures in the DO stadial/interstadial transition was identified as a regional phenomenon, which is likely induced by sea-ice feedbacks (Li et al., 2010; Deplazes et al., 2013). Given, the fact that the North Atlantic temperature and AMOC composite shown in Fig. 7 have already reached 2/3 of their full DO amplitude at zero lag whereas Greenland temperatures have only attained about 50 %, it may appear as if the Greenland record is lagging the other variables. This is merely a reflection of the nonlinearity of the Greenland temperature response. It should be noted here that this feature may impact the synchronization of high-resolution proxy timeseries with Greenland climate reconstructions.

According to our model and data-based evidence, we conclude that ice sheet-driven freshwater changes determined the abruptness of DO events, their "periodicity" and global teleconnections.

Acknowledgements. This project was supported by the Australian Research Council. Model experiments were performed on a computational cluster owned by the Faculty of Science of the University of New South Wales as well as on a cluster from the NCI National Facility at the Australian National University. T. Friedrich and A. Timmermann are supported by NSF grant #1010869 and by the Japan Agency for Marine-Earth Science and Technology (JAMSTEC) through its sponsorship of the International Pacific Research Center. M. England acknowledges funding from the ARC Laureate Fellowship program (FL100100214). We thank C. Jackson for providing his optimized freshwater forcing timeseries as well as M. Elliot and N. Thouveny for providing their data for comparisons. We are also grateful to S. Harrison for organizing a workshop at Macquarie University, that stimulated many interesting discussions on DO events.

References

Abe-Ouchi, A., Segawa, T., and Saito, F.: Climatic Conditions for modelling the Northern Hemisphere ice sheets throughout the ice age cycle, Clim. Past, 3, 423–438, doi:10.5194/cp-3-423-2007, 2007. 4775

Alley, R.: Ice-core evidence of abrupt climate changes, P. Natl. Acad. Sci. USA, 97, 1331–1334, 2000. 4786, 4796, 4806

Alvarez-Solas, J., Charbit, S., Ritz, C., Paillard, D., Ramstein, G., and Dumas, C.: Links between ocean temperature and iceberg discharge during Heinrich events, Nat. Geosci., 3, 122–126, doi:10.1038/NGEO752, 2010. 4774, 4785, 4805

Andersen, K., Svensson, A., Johnsen, S., Rasmussen, S., Bigler, M., Röthlisberger, R., Ruth, U., Siggaard-Andersen, M.-L., Steffensen, J., Dahl-Jensen, D., Vinther, B., and Clausen, H.: The Greenland ice core chronology 2005, 15–42 ka, Part 1: Constructing the time scale, Quaternary Sci. Rev., 25, 3246–3257, 2006. 4781, 4782, 4783, 4796, 4803

Barker, S., Diz, P., Vautravers, M., Pike, J., Knorr, G., Hall, I., and Broecker, W.: Interhemispheric Atlantic seesaw response during the last deglaciation, Nature, 457, 1097–1102, 2009. 4779

Blunier, T., Chappellaz, J., Schwander, J., Dällenbach, A., Stauffer, B., Stocker, T., Raynaud, D., Jouzel, J., Clausens, H., Hammer, C., and Johnsen, S.: Asynchrony of Antarctic and Greenland climate change during the last glacial period, Nature, 394, 739–743, 1998. 4779

Bond, G. and Lotti, R.: Iceberg discharges into the North Atlantic on millennial time scales during the last glaciation, Science, 267, 1005–1010, 1995. 4773, 4784, 4785

Broccoli, A., Dahl, K., and Stouffer, R.: Response of the ITCZ to Northern Hemisphere cooling, Geophys. Res. Lett., 33, L01702, doi:10.1029/2005GL024546, 2006. 4780

Brovkin, V., Ganopolski, A., and Svirezhev, Y.: A continuous climate-vegetation classification for use in climate-biosphere studies, Ecol. Model., 101, 251–261, 1997. 4775

Cane, M. A., Kamenkovich, V. M., and Krupitsky, A.: On the utility and disutility of JEBAR, J. Phys. Oceanogr., 28, 519–526, 1998. 4782

Capron, E., Landais, A., Chappellaz, J., Schilt, A., Buiron, D., Dahl-Jensen, D., Johnsen, S. J., Jouzel, J., Lemieux-Dudon, B., Loulergue, L., Leuenberger, M., Masson-Delmotte, V., Meyer, H., Oerter, H., and Stenni, B.: Millennial and sub-millennial scale climatic variations recorded in polar ice cores over the last glacial period, Clim. Past, 6, 345–365, doi:10.5194/cp-6-345-2010, 2010. 4779, 4781

Chapman, M. and Shackleton, N.: Global ice-volume fluctuations, North Atlantic ice-rafting events, and deep-ocean circulation changes between 130 and 70 ka, Geology, 27, 795–798, 1999. 4778

Dansgaard, W., Johnsen, S., and Clausen, H.: Evidence for general instability of past climate from a 250-kyr ice-core record, Nature, 364, 218–220, 1993. 4772

Deplazes, G., Lückge, A., Peterson, L., Timmermann, A., Hamann, Y., Hughen, K., Röh, U., Laj, C., Cane, M., Sigman, D., and Haug, G.: Links between tropical rainfall and North Atlantic climate during the last glacial period, Nat. Geosci., 6, 213–217, 2013. 4774, 4779, 4780, 4786, 4800, 4804

Eisenman, I., Bitz, C., and Tziperman, E.: Rain driven by receding ice sheets as a cause of past climate change, Paleoceanography, 24, PA4209, doi:10.1029/2009PA001778, 2009. 4774

Fleitmann, D., Cheng, H., Badertscher, S., Edwards, R., Mudelsee, M., Göktürk, O., Fankhauser, A., Pickering, R., Raible, C., Matter, A., Kramers, J., and Tüysüz, O.: Timing and climatic impact of Greenland interstadials recorded in stalagmites from northern Turkey, Geophys. Res. Lett., 36, L19707, doi:10.1029/2009GL040050, 2009. 4779, 4783, 4795, 4798

Flückiger, J., Knutti, R., and White, J.: Oceanic processes as potential trigger and amplifying mechanisms for Heinrich events, Paleoceanography, 21, PA2014, doi:10.1029/2005PA001204, 2006. 4785

Garcin, Y., Williamson, D., Taieb, M., Vincens, A., Mathé, P.-E., and Majule, A.: Centennial to millennial changes in maar-lake deposition during the last 45 000 years in tropical southern Africa (Lake Masoko, Tanzania), Palaeogeogr. Palaeocl., 239, 334–354, 2006. 4774

Godfrey, J.: A Sverdrup model of the depth-integrated flow from the world ocean allowing for island circulations, Geophys. Astro. Fluid, 45, 89–112, 1989. 4782

Goosse, H., Brovkin, V., Fichefet, T., Haarsma, R., Huybrechts, P., Jongma, J., Mouchet, A., Selten, F., Barriat, P.-Y., Campin, J.-M., Deleersnijder, E., Driesschaert, E., Goelzer, H., Janssens, I., Loutre, M.-F., Morales Maqueda, M. A., Opsteegh, T., Mathieu, P.-P., Munhoven, G., Pettersson, E. J., Renssen, H., Roche, D. M., Schaeffer, M., Tartinville, B., Timmermann, A., and Weber, S. L.: Description of the Earth system model of intermediate complexity LOVECLIM version 1.2, Geosci. Model Dev., 3, 603–633, doi:10.5194/gmd-3-603-2010, 2010. 4775

Grousset, F., Labeyrie, L., Sinko, J., Cremer, M., Bond, G., Duprat, J., Cortija, E., and Huon, S.: Patterns of ice-rafted detritus in the glacial North Atlantic (40–55° N), Paleoceanography, 8, 175–192, 1993. 4773, 4779

Heinrich, H.: Origin and consequences of cyclic ice rafting in the northeast Atlantic Ocean during the past 130 000 years, Quaternary Res., 29, 142–152, 1988. 4773

Hemming, S.: Heinrich events: massive late Pleistocene detritus layers of the North Atlantic and their global climate imprint, Rev. Geophys., 42, RG1005, doi:10.1029/2003RG000128, 2004. 4773, 4784

Hodell, D., Anselmetti, F., Ariztegui, D., Brenner, M., Curtis, J., Gilli, A., Grzesik, D., Guilderson, T., Müller, A., Bush, M., Correa-Metrio, A., Escobar, J., and Kutterolf, S.: An 85-ka record of climate change in lowland Central America, Quaternary Sci. Rev., 27, 1152–1165, 2008. 4780, 4801

Hodell, D., Evans, H., Channell, J., and Curtis, J.: Phase relationships of North Atlantic ice-rafted debris and surface-deep climate proxies during the last glacial period, Quaternary Sci. Rev., 29, 3875–3886, 2010. 4773, 4778

Huber, C., Leuenberger, M., Spahni, R., Flückiger, J., Schwander, J., Stocker, T., Johnsen, S., Landais, A., and Jouzel, J.: Isotope calibrated Greenland temperature record over Marine

Isotope Stage 3 and its relation to CH_4, Earth Planet. Sc. Lett., 243, 504–519, 2006. 4779, 4782, 4795, 4798
Jackson, C. S., Marchal, O., Liu, Y., Lu, S., and Thompson, W. G.: A box-model test of the freshwater forcing hypothesis of abrupt climate change and the physics governing ocean stability, Paleoceanography, 25, PA4222, doi:10.1029/2010PA001936, 2010. 4777
Kageyama, M., Merkel, U., Otto-Bliesner, B., Prange, M., Abe-Ouchi, A., Lohmann, G., Ohgaito, R., Roche, D. M., Singarayer, J., Swingedouw, D., and Zhang, X.: Climatic impacts of fresh water hosing under Last Glacial Maximum conditions: a multi-model study, Clim. Past, 9, 935–953, doi:10.5194/cp-9-935-2013, 2013. 4773, 4779, 4780
Kanner, L., Burns, S., Cheng, H., and Edwards, R. L.: High-latitude forcing of the South American summer monsoon during the last glacial, Science, 335, 570–573, 2013. 4774, 4781, 4783, 4795, 4801
Kissel, C., Laj, C., Piotrowski, A., Goldstein, S., and Hemming, S.: Millennial-scale propagation of Atlantic deep waters to the glacial southern Ocean, Paleoceanography, 23, PA2102, doi:10.1029/2008PA001624, 2008. 4773, 4778, 4797, 4803
Krebs, U. and Timmermann, A.: Tropical air-sea interactions accelerate the recovery of the Atlantic meridional overturning circulation after a major shutdown, J. Climate, 20, 4940–4956, 2007a. 4773
Krebs, U. and Timmermann, A.: Fast advective recovery of the Atlantic meridional overturning circulation after a Heinrich event, Paleoceanography, 22, PA1220, doi:10.1029/2005PA001259, 2007b. 4774
Li, C., Battisti, D., Schrag, D., and Tziperman, E.: Abrupt climate shifts in Greenland due to displacements of the sea ice edge, Geophys. Res. Lett., 32, L19702, doi:10.1029/2005GL023492, 2005. 4774, 4779
Li, C., Battisti, D., and Bitz, C.: Can North Atlantic sea ice anomalies account for Dansgaard–Oeschger climate signals?, J. Climate, 23, 5457–5475, 2010. 4774, 4786
Marcott, S., Clark, P., Padman, L., Klinkhammer, G., Springer, S., Liu, Z., Otto-Bliesner, B., Carlson, A., Ungerer, A., Padman, J., He, F., Cheng, J., and Schmittner, A.: Ice-shelf collapse from subsurface warming as trigger for Heinrich events, P. Natl. Acad. Sci. USA, 267, 13415–13419, doi:10.1073/pnas.1104772108, 2011. 4774, 4785
Margari, V., Skinner, L. C., Tzedakis, P. C., Ganopolski, A., Vautravers, M., and Shackleton, N. J.: The nature of millennial-scale climate variability during the past two glacial periods, Nat. Geosci., 3, 127–131, 2010. 4778

CPD
9, 4771–4806, 2013
MIS3 Heinrich and D/O
L. Menviel et al.

Marshall, S. J. and Koutnik, M.: Ice sheet action versus reaction: distinguishing between Heinrich events and Dansgaard–Oeschger cycles in the North Atlantic, Paleoceanography, 21, PA2021, doi:10.1029/2005PA001247, 2006. 4785
Martrat, B., Grimalt, J., Shackleton, N., de Abreu, L., Hutterli, M., and Stocker, T.: Four climate cycles of recurring deep and surface water destabilizations on the Iberian margin, Science, 317, 502–507, 2007. 4776, 4797, 4798, 4803
Menviel, L., Timmermann, A., Mouchet, A., and Timm, O.: Meridional reorganizations of marine and terrestrial productivity during Heinrich events, Paleoceanography, 23, PA1203, doi:10.1029/2007PA001445, 2008. 4775
Menviel, L., Timmermann, A., Mouchet, A., and Timm, O.: Climate and biogeochemical response to a rapid melting of the West-Antarctic Ice Sheet during interglacials and implications for future climate, Paleoceanography, 25, PA4231, doi:10.1029/2009PA001892, 2010. 4774
Mosblech, N., Bush, M., Gosling, W., Hodell, D., Thomas, L., van Calsteren, P., Correa-Metrio, A., Valencia, B., Curtis, J., and van Woesik, R.: North Atlantic forcing of Amazonian precipitation during the last ice age, Nat. Geosci., 5, 817–820, doi:10.1038/NGEO1588, 2012. 4781, 4783, 4795, 4801
Mouchet, A.: A 3D model of ocean biogeochemical cycles and climate sensitivity studies, Ph. D. thesis, Université de Liège, Lìege, Belgium, 2011. 4775
Nave, S., Labeyrie, L., Gherardi, J., Caillon, N., Cortija, E., Kissel, C., and Abrantes, F.: Primary productivty response to Heinrich events in the North Atlantic Ocean and Norwegian Sea, Paleoceanography, 22, PA3216, doi:10.1029/2006PA001335, 2007. 4779
Petersen, S., Schrag, D., and Clark, P.: A new mechanism for Dansgaard–Oeschger cycles, Paleoceanography, 28, 24–30, doi:10.1029/2012PA002364, 2013. 4774
Rashid, H., Hesse, R., and Piper, D.: Evidence for an additional Heinrich event between H5 and H6 in the Labrador Sea, Paleoceanography, 18, 1077, doi:10.1029/2003PA000913, 2003. 4779
Sarkisyan, A. and Ivanov, V. F.: Joint effect of baroclinicity and bottom relief as an important factor in the dynamics of sea currents, Izv. Acad. Sci. USSR, Atmos. Oceanic Phys., 7, 116–124, 1971 (in Russian). 4782
Sarnthein, M., Eystein, J., Weinelt, M., Arnold, M., Duplessy, J., Erlenkeuser, H., Flatoy, A., Johannessen, G., Johannessen, T., Jung, S., Koc, N., Labeyrie, L., Maslin, M., Pflaumann, U.,

CPD
9, 4771–4806, 2013
MIS3 Heinrich and D/O
L. Menviel et al.

and Schulz, H.: Variations in Atlantic surface ocean paleoceanography, 50–80° N: a time-slice record of the last 30 000 years, Paleoceanography, 10, 1063–1094, 1995. 4773
Sarnthein, M., Stattegger, K., Dreger, D., Erlenkeuser, H., Grootes, P., Haupt, B., Jung, S., Kiefer, T., Kuhnt, W., Pflaumann, U., Schäfer-Neth, C., Schulz, H., Schulz, M., Seidov, D., Simstich, J., van Kreveld, S., Vogelsang, E., Völker, A., and Weinelt, M.: Fundamental modes and abrupt changes in North Atlantic circulation and climate over the last 60 ky – concepts, reconstruction and numerical modeling, in: The Northern North Atlantic: A Changing Environment, Springer, Berlin, 365–410, 2001. 4773, 4783, 4784, 4785
Schönfeld, J., Zahn, R., and de Abreu, L.: Surface to deep water response to rapid climate changes at the western Iberian Margin, Global Planet. Change, 36, 237–264, 2003a. 4778
Schönfeld, J., Zahn, R., and de Abreu, L.: Surface and deep water response to rapid climate changes at the western Iberian Margin, Global Planet. Change, 36, 237–264, 2003b. 4773
Schoof, C.: Ice sheet grounding line dynamics: steady states, stability, and hysteresis, J. Geophys. Res., 112, F03S28, doi:10.1029/2006JF000664, 2007. 4774
Schulz, M., Berger, W., Sarnthein, M., and Grootes, P.: Amplitude variations of 1470-year climate oscillations during the last 100 000 years linked to fluctuations of continental ice mass, Geophys. Res. Lett., 22, 3385–3388, 1999. 4774
Shaffer, G., Olsen, S., and Bjerrum, C.: Ocean subsurface warming as a mechanism for coupling Dansgaard–Oeschger climate cycles and ice-rafting events, Geophys. Res. Lett., 31, L24202, doi:10.1029/2004GL020968, 2004. 4774, 4785
Siddall, M., Rohling, E., Almogi-Labin, A., Hemleben, C., Meischner, D., Schmelzer, I., and Smeed, D.: Sea-level fluctuations during the last glacial cycle, Nature, 423, 853–858, 2003. 4778
Steffensen, J., Andersen, K., Bigler, M., Clausen, H., Dahl-Jensen, D., Fischer, H., Goto-Azuma, K., Hansson, M., Johnsen, S., Jouzel, J., Masson-Delmotte, V., Popp, T., Rasmussen, S., Röthlisberger, R., Ruth, U., Stauffer, B., Siggaard-Andersen, M.-L., Sveinbjörnsdóttir, A., Svensson, A., and White, J.: High-resolution Greenland ice core data show abrupt climate change happens in few years, Science, 321, 680–684, 2008. 4781
Stenni, B., Buiron, D., Frezzotti, M., Albani, S., Barbante, C., Bard, E., Barnola, J., Baroni, M., Baumgartner, M., Bonazza, M., Capron, E., Castellano, E., Chappellaz, J., Delmonte, B., Falourd, S., Genoni, L., Iacumin, P., Jouzel, J., Kipfstuhl, S., Landais, A., Lemieux-Dudon, B., Maggi, V., Masson-Delmotte, V., Mazzola, C., Minster, B., Montagnat, M., Mulvaney, R., Narcisi, B., Oerter, H., Parrenin, F., Petit, J., Ritz, C., Scarchilli, C., Schilt, A., Schüpbach, S.,

CPD
9, 4771–4806, 2013
MIS3 Heinrich and D/O
L. Menviel et al.

Schwander, J., Selmo, E., Severi, M., Stocker, T., and Udisti, R.: Expression of the bipolar see-saw in Antarctic climate records during the last deglaciation, Nat. Geosci., 4, 46–49, 2011. 4774, 4779

Stocker, T.: The seesaw effect, Science, 282, 61–62, 1998. 4780

Stocker, T. and Johnsen, S.: A minimum thermodynamic model for the bipolar seesaw, Paleoceanography, 18, 1087, doi:10.1029/2003PA000920, 2003. 4780

Stouffer, R., Yin, J., Gregory, J., Dixon, K., Spelman, M., Hurlin, W., Weaver, A., Eby, M., Flato, G., Hasumi, H., Hu, A., Jungclaus, J., Kamenkovich, I., Levermann, A., Montoya, M., Murakami, S., Nawrath, S., Oka, A., Peltier, W., Robitaille, D., Sokolov, A., Vettoretti, G., and Weber, S.: Investigating the causes of the response of the thermohaline circulation to past and future climate changes, J. Climate, 19, 1365–1387, 2006. 4779

Stouffer, R., Seidov, D., and Haupt, B.: Climate response to external sources of freshwater: North Atlantic versus the Southern Ocean, J. Climate, 20, 436–448, 2007. 4773, 4779

Svensson, A., Andersen, K., Bigler, M., Clausen, H. B., Dahl-Jensen, D., Davies, S. M., Johnsen, S. J., Muscheler, R., Rasmussen, S. O., Röthlisberger, R., Steffensen, J. P., and Vinther, B. M.: The Greenland ice core chronology 2005, 15–42 ka, Part 2: Comparison to other records, Quaternary Sci. Rev., 25, 3258–3267, 2006. 4781, 4782, 4796, 4803

Timm, O. and Timmermann, A.: Simulation of the last 21 000 years using accelerated transient boundary conditions, J. Climate, 20, 4377–4401, 2007. 4775

Timm, O., Timmermann, A., Abe-Ouchi, A., and Segawa, T.: On the definition of paleo-seasons in transient climate simulations, Paleoceanography, 23, PA2221, doi:10.1029/2007PA001461, 2008. 4775

Timmermann, A., Schulz, M., Gildor, H., and Tziperman, E.: Coherent resonant millennial-scale climate oscillations triggered by massive meltwater pulses, J. Climate, 16, 2569–2585, 2003. 4774

Timmermann, A., An, S. I., Krebs, U., and Goosse, H.: ENSO suppression due to a weakening of the North Atlantic thermohaline circulation, J. Climate, 18, 3122–3139, 2005a. 4782

Timmermann, A., Krebs, Justino, F., Goosse, H., and Ivanochko, T.: Mechanisms for millennial-scale global synchronization during the last glacial period, Paleoceanography, 20, PA4008, doi:10.1029/2004PA001090, 2005b. 4781

Timmermann, A., Okumura, Y., An, S.-I., Clement, A., Dong, B., Guilyardi, E., Hu, A., Jungclaus, J., Krebs, U., Renold, M., Stocker, T., Stouffer, R., Sutton, R., Xie, S.-P., and Yin, J.:

The influence of shutdown of the Atlantic meridional overturning circulation on ENSO, J. Climate, 19, 4899–4919, 2007. 4780
Timmermann, A., Menviel, L., Okumura, Y., Schilla, A., Merkel, U., Hu, A., Otto-Bliesner, B., and Schulz, M.: Towards a quantitative understanding of millennial-scale Antarctic warming events, Quaternary Sci. Rev., 29, 74–85, doi:10.1016/j.quascirev.2009.06.021, 2009a. 4779
Timmermann, A., Timm, O., Stott, L., and Menviel, L.: The roles of CO_2 and orbital forcing in driving southern hemispheric temperature variations during the last 21 000 yr, J. Climate, 22, 1626–1640, 2009b. 4775
van Kreveld, S., Samthein, M., Erlenkeuser, H., Grootes, P., Jung, S., Nadeau, M., Pflaumann, U., and Voelker, A.: Potential links between surging ice sheets, circulation changes, and the Dansgaard–Oeschger cycles in the Irminger Sea, 60–18 kyr, Paleoceanography, 15, 425–442, 2000. 4773, 4774, 4778, 4782, 4785, 4796, 4803, 4806
Vidal, L., Labeyrie, L., Cortijo, E., Arnold, M., Duplessy, J., Michel, E., Becque, S., and van Weering, T.: Evidence for changes in the North Atlantic Deep Water linked to meltwater surges during the Heinrich events, Earth Planet. Sc. Lett., 146, 13–27, 1997. 4773
Vidal, L., Schneider, R., Marchal, O., Bickert, T., Stocker, T., and Wefer, G.: Link between the North and South Atlantic during the Heinrich events of the last glacial period, Clim. Dynam., 15, 909–919, 1999. 4784
Voelker, A., Grootes, P. M., Nadeau, M.-J., and Sarnthein, M.: Radiocarbon levels in the Iceland sea from 25–53 kyr and their link to the earth's magnetic field intensity, Radiocarbon, 42, 437–452, 2000. 4773, 4796, 4806
Wang, X., Auler, A., Edwards, R., Cheng, H., Ito, E., Wang, Y., Kong, X., and Solheid, M.: Millennial-scale precipitation changes in southern Brazil over the past 90 000 years, Geophys. Res. Lett., 34, L23701, doi:10.1029/2007GL031149, 2007. 4774, 4781, 4801
Wang, Y., Cheng, H., Edwards, R., An, Z., Wu, J., Shen, C., and Dorale, J.: A high-resolution absolute-dated Late Pleistocene monsoon record from Hulu Cave, China, Science, 294, 2345–2348, 2001. 4774, 4780, 4783, 4795, 4800
Wunsch, C.: Abrupt climate change: an alternative view, Quaternary Res., 65, 191–203, 2006. 4774
Zahn, R., Schönfeld, J., Kudrass, H.-R., Park, M.-H., Erlenkeuser, H., and Grootes, P.: Thermohaline instability in the North Atlantic during meltwater events: Stable isotope and ice-rafted detritus records from core SO75-26KL, Portuguese margin, Paleoceanography, 12, 696–710, 1997. 4773

CPD
9, 4771–4806, 2013

Table 1. Table showing the timing of stadials H5, H4, C7/H3.2 and HS3 as recorded in high resolution well-dated paleorecords. We calculate the mean (ka BP, bold) and one standard deviation (ka) of the timing of each event as well as the duration (yr) of each event and its standard deviation (yr). In the Pacupahuain record, the two peaks around H5 were treated as a single event. A similar method was used for H3 in the Hulu cave record.

Paleoproxy record	H5 ka BP	H4 ka BP	C7/H3.2 ka BP	H3 ka BP	Ref.
Greenland $\delta^{18}O$ (GICC05)	48.8–46.9	39.95–38.25	36.65–35.5	32–28.9	Huber et al. (2006)
Sofular cave $\delta^{18}O$	48.8–47.7	39.9–38.2	36.6–35.95	31.5–29.5	Fleitmann et al. (2009)
Pacupahuain cave $\delta^{18}O$	48.7–48.2 48.0–47.45	40.4–38.4	36.4–35.8	30.5–28.9	Kanner et al. (2013)
Santiago cave $\delta^{18}O$	49–48.2	40.1–38.6	36.6–35.6	–	Mosblech et al. (2012)
Hulu cave $\delta^{18}O$	48.8–47.6	39.8–38.1	36–35.2	31.3–29.8 28.8–27.9	Wang et al. (2001)
Mean (ka BP)	**48.8–47.6**	**40.0–38.3**	**36.45–35.6**	**31.3–28.8**	
Standard deviation (ka)	0.1–0.5	0.2–0.2	0.2–0.3	0.5–0.6	
Duration (yr)	1250	1720	840	1820	
Standard deviation (yr)	360	160	210	730	

CPD
9, 4771–4806, 2013

MIS3 Heinrich and D/O

L. Menviel et al.

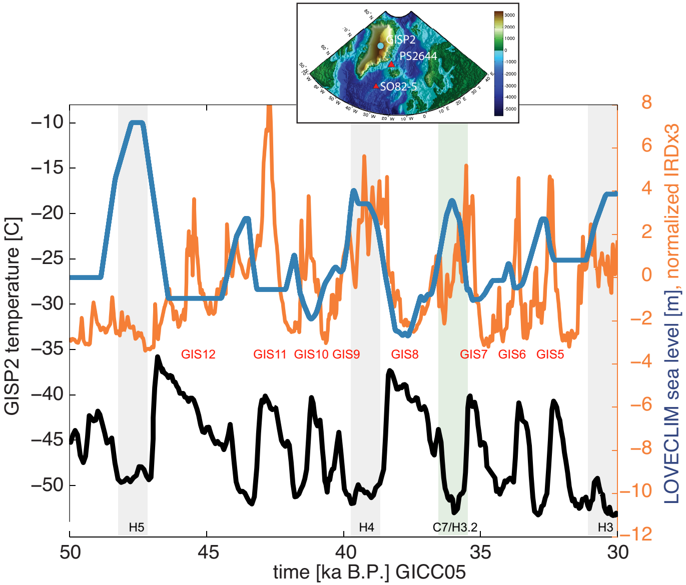

Fig. 1. Upper panel: composite IRD record (orange) obtained from the average of the normalized IRD records of SO82-5 (van Kreveld et al., 2000) and PS2644 (Voelker et al., 2000) from the northern North Atlantic (see map inlay). Integral of freshwater flux forcing used in the LOVECLIM MIS3 hindcast simulation (blue) (see Fig. 2, upper panel). Lower panel: GISP2 reconstructed Central Greenland temperatures (Alley, 2000). Greenland interstadials (GIS) are highlighted by red labels. The main Heinrich events are represented by gray bars and the light green bar marks the Greenland stadial C7 just prior to GIS7. The age-shift between the GISP2 record (Alley, 2000) and the NGRIP record on the GICC05 timescale (Andersen et al., 2006; Svensson et al., 2006) is determined. To project the paleorecords onto the common GICC05 age model, we apply this shift to the GISP2 record and to IRD records of cores SO82-5 and PS2644, whose original age models were partly based on correlations with GISP2. Subsequently the IRD composite (orange) was calculated.

CPD
9, 4771–4806, 2013

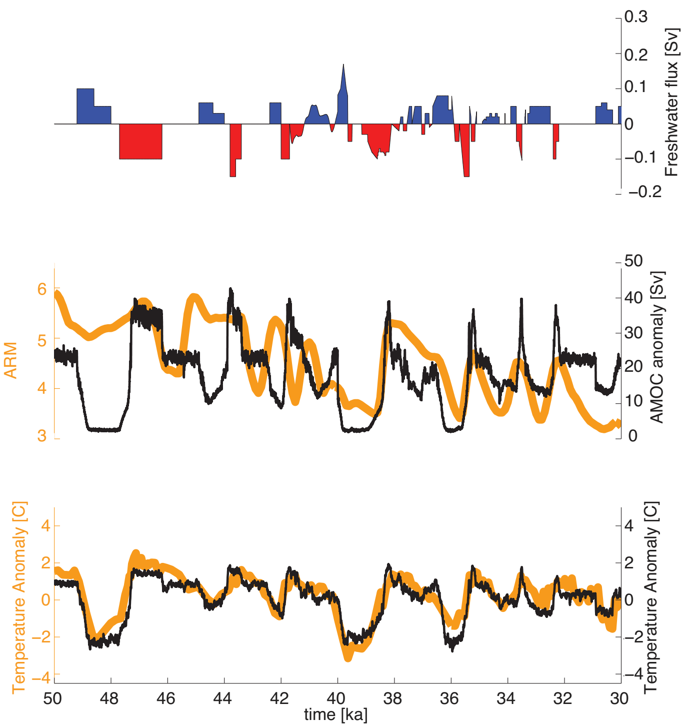

Fig. 2. From top to bottom: timeseries of North Atlantic freshwater forcing (Sv) applied to LOVECLIM in the region 55° W–10° W, 50° N–65° N; simulated maximum meridional overturning circulation in the North Atlantic (Sv) compared to North Atlantic marine sediment cores ARM data (Kissel et al., 2008); and simulated SST anomalies off the Iberian margin (15° W–8° W, 37° N–43° N) compared to alkenone-based SST anomalies from marine sediment core MD01-2444 (Martrat et al., 2007). Model results are in black and paleoproxy records in orange.

CPD
9, 4771–4806, 2013

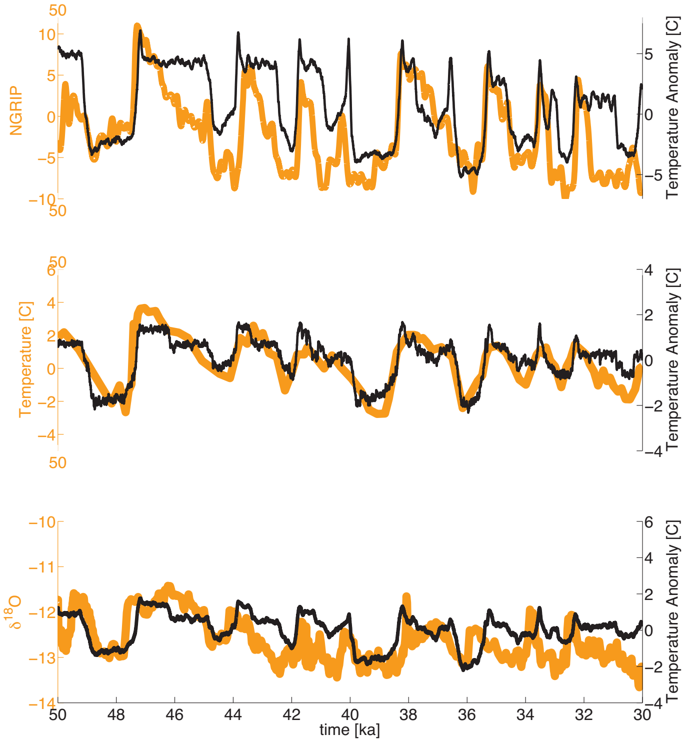

Fig. 3. From top to bottom: timeseries of simulated NE Greenland air temperature anomalies (40° W–10° E, 66° N–85° N) compared to the NGRIP temperature reconstruction (Huber et al., 2006); simulated SST in the western Mediterranean compared to alkenone-based SST reconstructions from the Alboran Sea ODP hole 161–977 A (Martrat et al., 2007) and simulated air temperature anomalies over Turkey (25° E–46° E, 35° N–42° N) compared to a speleothem δ^{18}O record (permil) from Sofular cave, Turkey (Fleitmann et al., 2009). Model results are in black and paleoproxy records in orange.

CPD
9, 4771–4806, 2013

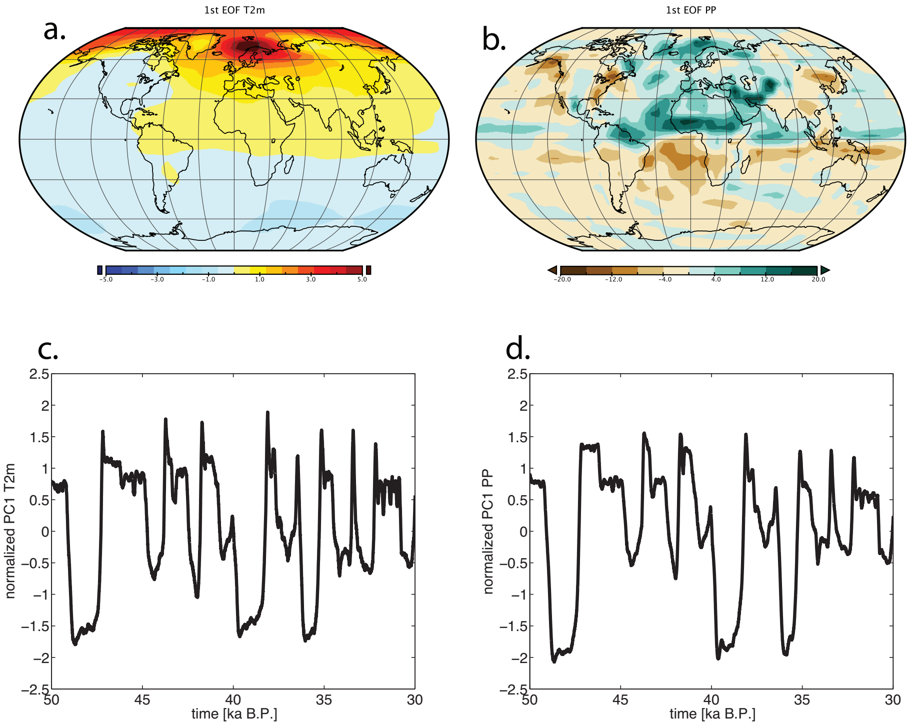

Fig. 4. (a) pattern of first EOF of detrended 2 m air temperature anomalies (°C); **(b)** pattern of first EOF of detrended precipitation anomalies ($cm\,yr^{-1}$); **(c)** normalized principal component of 1st EOF of detrended 2 m air temperature, which explains 64 % of the variance; **(d)** normalized principal component of 1st EOF of detrended precipitation, which explains 16 % of the variance.

CPD
9, 4771–4806, 2013
MIS3 Heinrich and D/O
L. Menviel et al.

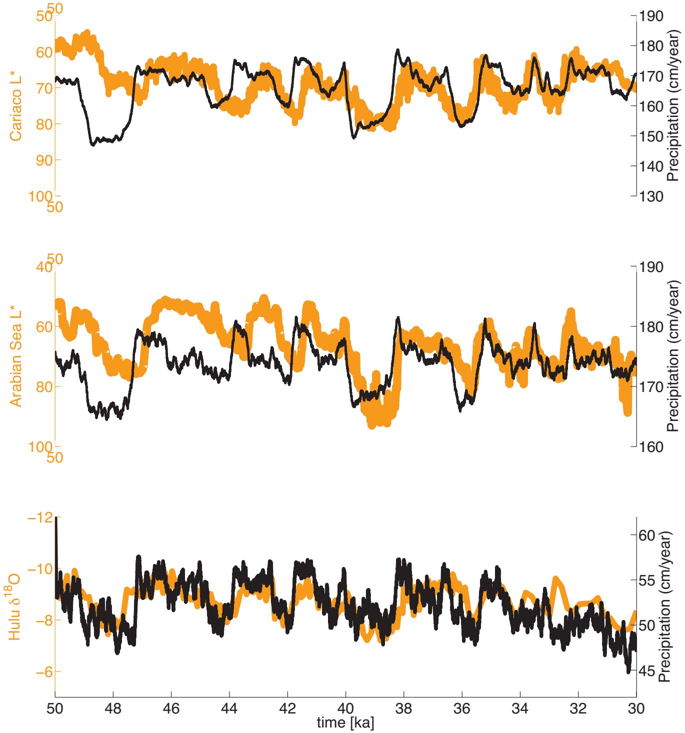

Fig. 5. From top to bottom: time series of simulated annual precipitation anomalies over the Cariaco basin (60° W–50° W, 5° N–20° N) compared to a reflectance record from the Cariaco basin (Deplazes et al., 2013); time series of simulated Arabian Sea annual precipitation (45° E–65° E, 5° N–15° N) compared to a reflectance record (L^*) from the northeastern Arabian Sea (Deplazes et al., 2013); simulated precipitation in eastern China (114° E–124° E, 28° N–35° N) compared to a speleothem δ^{18}O record (‰) from Hulu cave, China (Wang et al., 2001). Model results are in black and paleoproxy records in orange.

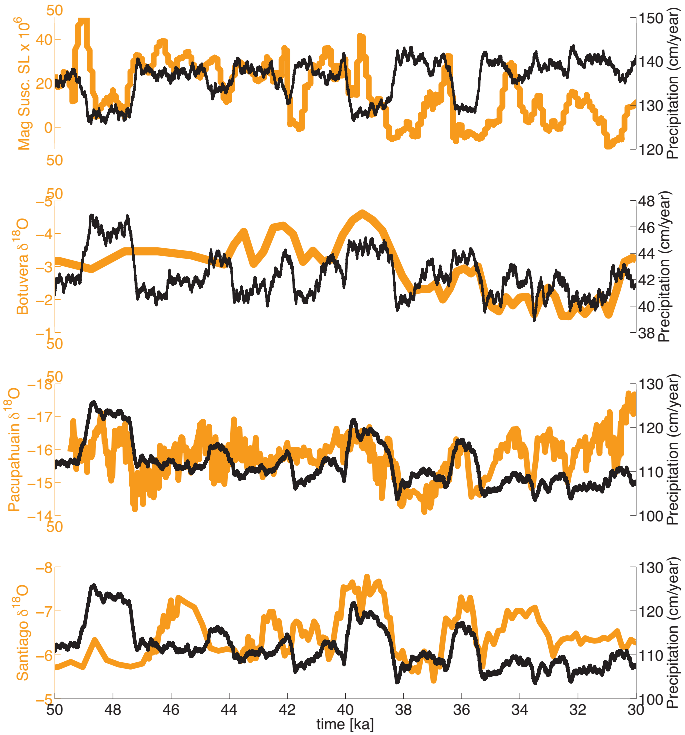

Fig. 6. From top to bottom: time series of simulated annual precipitation anomalies over Guatemala (104° W–93° W, 12° N–30° N) compared to a magnetic susceptibility record from Lake Peten Itza, Guatemala (Hodell et al., 2008); Brazil (44° W–60° W, 20° S–30° S) compared to $\delta^{18}O$ (‰) of a speleothem record from Botuvera cave, Brazil (Wang et al., 2007); Peru and Ecuador (85° W–70° W, 3° S–15° S) compared to speleothems $\delta^{18}O$ records from Pacupahuain cave, Peru (Kanner et al., 2013) and Santiago cave, Ecuador (Mosblech et al., 2012). Model results are in black and paleoproxy records in orange.

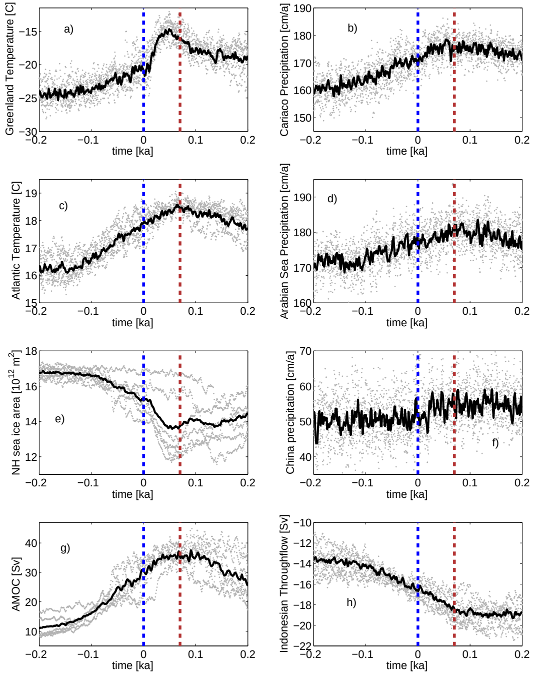

Fig. 7. Composite (thick black line) of DO stadial/interstadial transitions showing different simulated variables relative to the maximum time derivative in simulated Greenland temperatures occurring at 47.25, 43.9, 41.8, 38.3, 35.3, 33.6 and 32.34 ka BP: **(a)** Greenland air temperature, **(b)** Cariaco Basin precipitation, **(c)** North Atlantic temperature, **(d)** Arabian Sea precipitation, **(e)** Northern Hemisphere sea-ice area, **(f)** eastern China precipitation, **(g)** maximum of meridional streamfunction in North Atlantic, **(h)** strength of Indonesian Throughflow. The blue and red dashed lines respectively represent the time of the largest positive time-derivative of Greenland temperatures and the time when North Atlantic temperatures attain the maximum value. The gray dots represent the individual data points before calculating the composite.

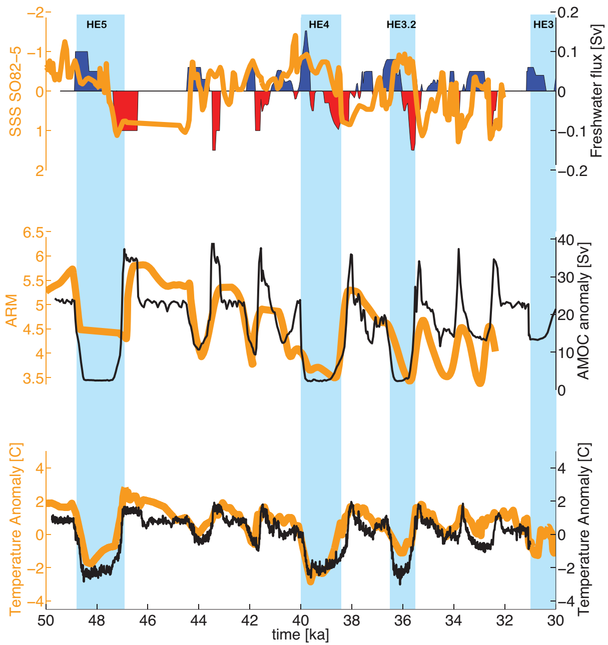

Fig. 8. From top to bottom: timeseries projected onto GICC05 age scale (Andersen et al., 2006; Svensson et al., 2006) of applied North Atlantic freshwater forcing (Sv) and Nordic Sea salinity from core S082-5 (van Kreveld et al., 2000); simulated maximum meridional overturning circulation in the North Atlantic (Sv) compared to North Atlantic marine sediment cores ARM data (Kissel et al., 2008); simulated SST anomalies off the Iberian margin (15° W–8° W, 37° N–43° N) compared to alkenone-based SST anomalies from marine sediment core MD01-2444 (Martrat et al., 2007). Model results are in black and paleoproxy records in orange.

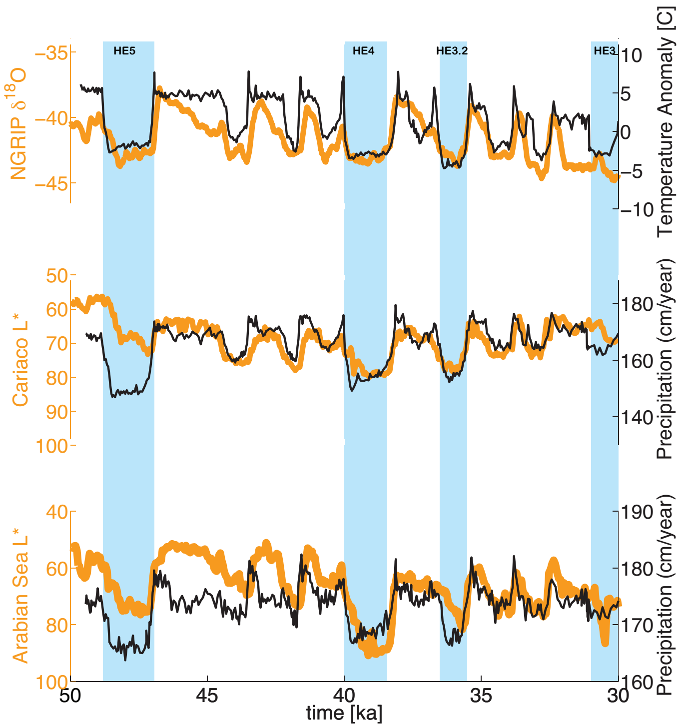

Fig. 9. From top to bottom: timeseries projected onto GICC05 age scale of simulated NE Greenland air temperature anomalies (40° W–10° E, 66° N–85° N) and NGRIP δ^{18}O; simulated annual precipitation anomalies over the Cariaco basin (60° W–50° W, 5° N–20° N) compared to a reflectance record from the Cariaco basin (Deplazes et al., 2013); time series of simulated Arabian Sea annual precipitation (45° E–65° E, 5° N–15° N) compared to a reflectance record (L^*) from the northeastern Arabian Sea (Deplazes et al., 2013). Model results are in black and paleoproxy records in orange.

CPD
9, 4771–4806, 2013

MIS3 Heinrich and D/O

L. Menviel et al.

Title Page
Abstract | Introduction
Conclusions | References
Tables | Figures
◀| |▶
◀ ▶
Back | Close
Full Screen / Esc
Printer-friendly Version
Interactive Discussion

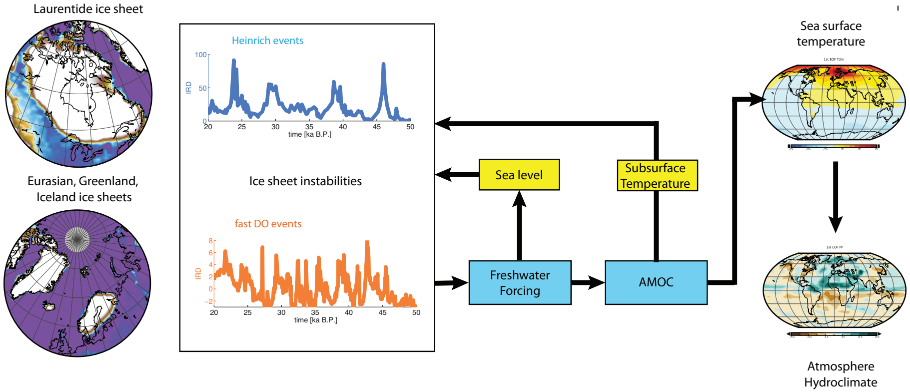

Fig. 10. Schematic illustration of the effect of the Northern Hemisphere ice sheet instabilities on the AMOC, SST and atmospheric circulation. AMOC changes are likely to provide a positive feedback on ice sheet instabilities via subsurface temperature anomalies (Alvarez-Solas et al., 2010). Furthermore, sea level changes generated by one ice sheet can trigger ice shelf instabilities in another ice sheet and subsequent accelerated flow and iceberg calving. Once the ice sheets reach a new mass-balance, the freshwater input into the North Atlantic ceases and the AMOC starts its recovery thus initiating a stadial/interstadial DO transition.

CPD
9, 4771–4806, 2013

L. Menviel et al.

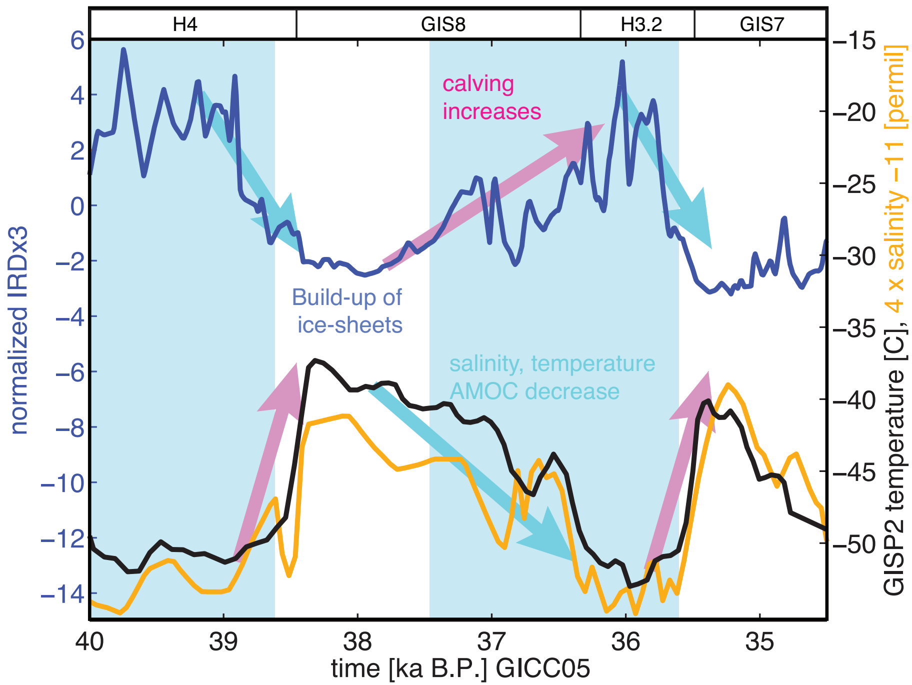

Fig. 11. Top: Composite IRD record (blue) obtained from the average of the normalized Northern North Atlantic IRD records SO82-5 (van Kreveld et al., 2000) and PS2644 (Voelker et al., 2000) (see Fig. 1); Bottom: GISP2 reconstructed Central Greenland temperatures (Alley, 2000) (black) and Irminger Sea sea surface salinities (orange) from SO82-5 (van Kreveld et al., 2000). All data are displayed on the GICC05 timescale (see Fig. 1).

CPD
9, 4771–4806, 2013